PAPER • OPEN ACCESS

Superconducting flux qubit capacitively coupled to an LC resonator

To cite this article: T Yamamoto *et al* 2014 *New J. Phys.* **16** 015017

View the article online for updates and enhancements.

You may also like

- Effective Hamiltonians for interacting superconducting qubits: local basis reduction and the Schrieffer–Wolff transformation
  Gioele Consani and Paul A Warburton

- Current biased gradiometric flux qubit in a circuit-QED architecture
  Mun Dae Kim

- Superconducting qubit-resonator-atom hybrid system
  Deshui Yu, Leong Chuan Kwek, Luigi Amico et al.

Superconducting flux qubit capacitively coupled to an LC resonator

T Yamamoto[1,2,5]**, K Inomata**[2]**, K Koshino**[3]**, P-M Billangeon**[2]**,
Y Nakamura**[2,4] **and J S Tsai**[1,2]

[1] NEC Smart Energy Research Laboratories, Tsukuba, Ibaraki 305-8501, Japan
[2] RIKEN Center for Emergent Matter Science, Wako, Saitama 351-0198, Japan
[3] College of Liberal Arts and Sciences, Tokyo Medical and Dental University,
2-8-30 Konodai, Ichikawa 272-0827, Japan
[4] Research Center for Advanced Science and Technology, The University of Tokyo,
Meguro-ku, Tokyo 153-8904, Japan
E-mail: t-yamamoto@fe.jp.nec.com

Abstract

We study the system where a superconducting flux qubit is capacitively coupled
to an LC resonator. In three devices with different coupling capacitance, the
magnitude of the dispersive shift is enhanced by the third level of the qubit and
quantitatively agrees with the theory. We show by numerical calculation that the
capacitive coupling plays an essential role for the enhancement in the dispersive
shift. We investigate the coherence properties in two of these devices, which
are in the strong-dispersive regime, and show that the qubit energy relaxation
is currently not limited by the coupling. We also observe the discrete ac-Stark
effect, a hallmark of the strong-dispersive regime, in accordance with the theory.

1. Introduction

Dispersive readout is widely used for superconducting qubits, because it potentially enables
high-fidelity, fast and non-destructive readout [1]. In this readout scheme, the superconducting
qubits are coupled to an electromagnetic resonator (LC resonator) or transmission line, and the

[5] Author to whom any correspondence should be addressed.

type of coupling, i.e. what kind of degree of freedom to use, and its strength should be properly chosen based on various aspects, such as readout fidelity and backaction on the qubits. Note that even for the same type of qubit, we can still choose either capacitive (voltage) or inductive (current) coupling. For example, in charge (or transmon) and phase qubits, both capacitive and inductive couplings have been studied [2–6]. Transmon and phase qubits are (dc-) charge insensitive devices. However, as pointed out by Koch *et al* [7], this does not mean they are insensitive to the ac voltage field, and the strong coupling regime has indeed been achieved in these devices using capacitive coupling [2, 8].

For the superconducting flux qubits, on the other hand, inductive coupling has typically been used [9, 10]. This may be related to the fact that the states of the flux qubit are often associated with the clockwise and the counterclockwise circulating currents, besides that the flux qubits are also (dc-) charge insensitive devices. Again, however, this does not mean that capacitive coupling is impossible for the flux qubits[6]. We demonstrated in [13] that we can achieve strong coupling between a conventional flux qubit and an LC resonator coupled via a capacitance. In the paper, we also reported an enhancement of the dispersive shift of the cavity resonance induced by the third level of the flux qubit. This effect was first predicted for the transmon qubit [7] to occur when a specific level configuration, $\omega_{01} < \omega_{\mathrm{r}} < \omega_{12}$, is realized, where ω_{ij} is the qubit transition frequency between the ith and the jth levels and ω_{r} is the cavity resonant frequency. They call this a *straddling regime*, in which cooperative interplay between 0–1 and 1–2 transitions gives rise to the enhancement of the dispersive shift. In [13], we show that the magnitude of the observed dispersive shift, which was more than four times larger than that estimated from a simple two-level approximation, is quite consistent with the theory which takes into account the higher levels of the flux qubit. We note that the effect of the higher levels of the artificial atom on the dispersive shift has recently been investigated in the fluxonium qubit too [14, 15].

The present paper is an extension of our previous paper [13] and motivated mainly by the following three questions related to the enhancement in the dispersive shift. (i) Why had such a large enhancement never been observed in much more extensively studied devices with inductive coupling? (ii) Does the enhanced dispersive shift affect the coherence of the qubit? (iii) Can the enhanced dispersive shift be applied to anything besides the readout of the qubit? To answer these questions, the rest of the present paper is organized as follows: in section 2, we describe the details of the sample fabrication and the measurements. In the present paper, we study three different devices. In all the devices, a flux qubit is coupled to an LC resonator, but with different magnitude of the coupling capacitance. In section 3, we measure the dispersive shift in the three devices, and compare it with the calculation using the device parameters independently determined by the spectroscopy measurements. Section 4 is related to the first question. We calculate the energy band of the two circuits in the straddling regime, where the flux qubit is coupled to a resonator either via a capacitance or an inductance. Based on that, we discuss the difference in the enhancement of the dispersive shift. Section 5 is to answer the second question, in which we study the coherence property of our devices. The results show that the energy relaxation time is not limited by the coupling at present. Section 6 is related to the third question, where we clearly observe the discrete ac-Stark effect, which is a hallmark

---

[6] Capacitive coupling for a capacitively shunted flux qubit has been demonstrated in [11]. Also, it has been theoretically shown that high-frequency charge noise can induce substantial energy relaxation in flux qubits [12].
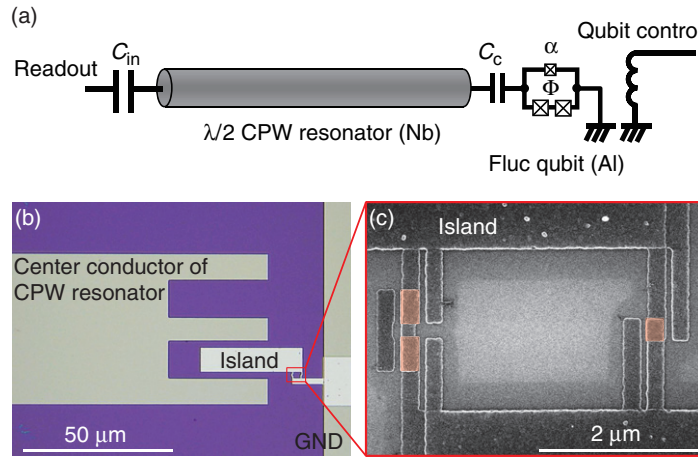
Figure 1. (a) Schematic representation of the device. A 3JJ flux qubit, in which one of the three junctions is smaller than the others by a factor of α, is coupled to a center conductor of $\lambda/2$-type CPW resonator via a capacitance C_c. The magnetic flux Φ penetrates the loop of the flux qubit, which is inductively coupled to the control line. The resonator is also coupled to an external transmission line for the readout via a capacitance C_{in}. (b) Optical image of the device with C_c of 4 fF magnified for the qubit part. (c) Scanning electron micrograph of the three-junction flux qubit. The areas shaded by red represent the Josephson junctions.

of the strong-dispersive regime. We show that the data are well reproduced by the theory. Finally, in section 7, we summarize our results.

2. Sample fabrication and measurements

In this work, we study the system where a superconducting flux qubit is capacitively coupled to a superconducting coplanar waveguide (CPW) resonator (figure 1). The CPW resonator is made of a 50 nm thick Nb film sputtered on a 300 μm thick undoped Si wafer covered by a 300 nm thick thermal oxide. It is patterned by electron-beam (EB) lithography using the ZEP520A-7 resist and CF$_4$ reactive ion etching. The flux qubit is a conventional three-Josephson-junction (3JJ) flux qubit, in which one junction is made smaller than the other two by a factor of α. It is fabricated by EB lithography and double-angle evaporation of Al using PMMA/Ge/MMA trilayer resist. The thicknesses of the bottom and the top Al layers are 20 and 30 nm, respectively. In order to realize a superconducting contact between Nb and Al, the surface of Nb is cleaned by Ar ion milling before the evaporation of Al.

In this work, we study the three devices with different coupling capacitances C_c between the qubit and the resonator. We call them devices A, B and C, which have designed C_c of 2, 3 and 4 fF, respectively. All of the devices have a $\lambda/2$-type CPW resonator of the same design. They have the fundamental resonant frequency at around 10.25 GHz, and the loaded quality factor Q of $\sim$650, which is limited by the input capacitance C_{in} designed to be 15 fF. The qubits have almost the same design in all of the devices, but with small adjustment in α to compensate for the effect of C_c on ω_{01}. The loop has a size of $\sim 2.0 \times 2.4\,\mu$m^2, and is coupled to the control line by a mutual inductance of ~ 0.1 pH.
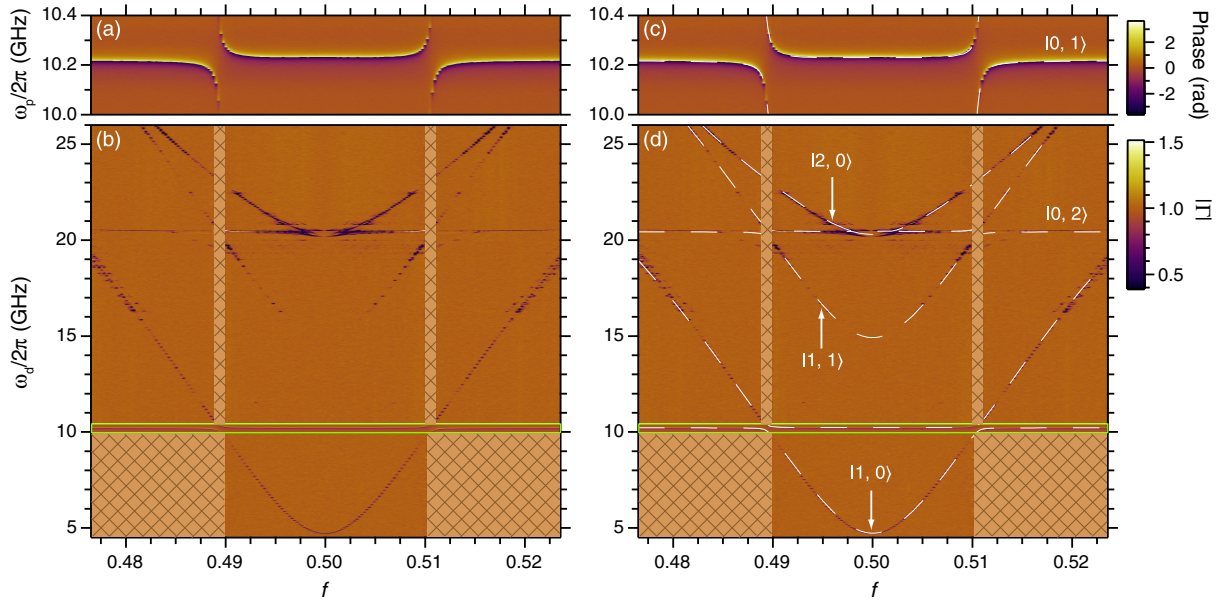
Figure 2. Spectroscopy of the coupled system (device B). (a) Phase of the reflection coefficient Γ as a function of the flux bias and the probe frequency. (b) $|\Gamma|$ as a function of the flux bias and the qubit excitation frequency. $|\Gamma|$ is normalized by the value measured at ω_r without the qubit drive. The same data as in (a) are shown in the green box for comparison. There are no data in the regions filled with the meshes. Panels (c) and (d) are the same as (a) and (b), respectively, but the result of the fitting is overlaid by the white dashed curves. Labels on the energy levels denote the corresponding excitation from the ground state, namely, $|q, r\rangle$ indicates that the qubit and the resonator are in the qth and the rth states, respectively.

The devices were mounted in a sample holder made of gold-plated copper, which is thermally anchored to the mixing chamber of a dilution refrigerator and cooled to $\sim 10\,\mathrm{mK}$. The sample holder is covered by three-layer (one superconducting and two μ-metal) magnetic shields, but we do not use radar-absorbent materials [16] in this work. For the spectroscopy measurements, we used a vector network analyzer. For the measurements of the dispersive shift and qubit coherence, we used a pulsed microwave and for the heterodyne detection of the time-domain data we used a commercial analogue-to-digital converter [13].

3. Dispersive shift in the straddling regime

Before investigating the dispersive shift, we need to experimentally determine the device parameters. As shown in [13], this was done by probing the energy bands of the system by the spectroscopy measurements and fitting the result with the energy bands calculated from the model Hamiltonian (equations (1)–(4) in the next section). Figure 2 shows an example of the spectroscopy measurement for device B. In figure 2(a), we plot the phase of the reflection coefficient Γ as a function of the probe frequency ω_p and the flux bias for the qubit $f \equiv \Phi/\Phi_0$, where Φ is the flux through the qubit loop and Φ_0 is the flux quantum. We observe clear vacuum Rabi splitting indicating that the strong coupling regime is achieved. In figure 2(b), on the other hand, we measure Γ at a fixed probe frequency $\omega_p = \omega_r = 2\pi \times 10.274\,\mathrm{GHz}$, where ω_r is the
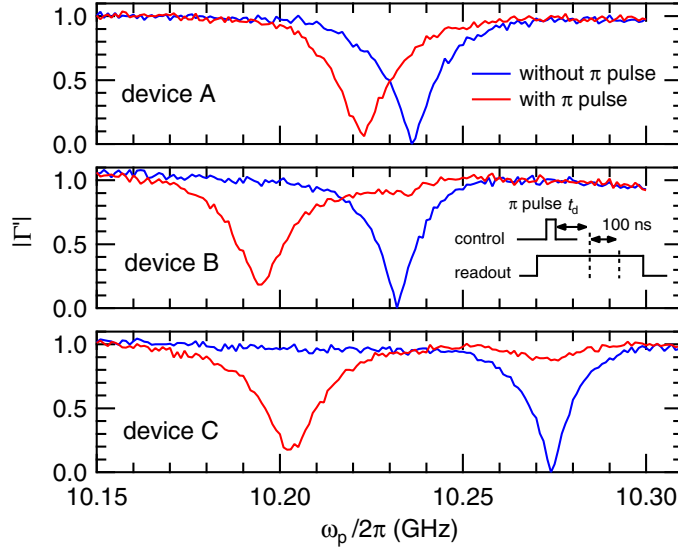
Figure 3. Dispersive shifts in all of the devices. The normalized reflection coefficient $|\Gamma'|$ is plotted as a function of the frequency of the probe microwave field ω_p. Blue (red) traces represent $|\Gamma'|$ when the π pulse is turned off (on). The inset shows the sequence of the pulses applied to measure $|\Gamma'|$.

resonant frequency of the resonator when the qubit is in state $|0\rangle$, while applying an additional continuous microwave field at ω_d to the qubit control port. In the figure, $|\Gamma|$ is plotted as a function of ω_d and f. Figures 2(c) and (d) are the same as figures 2(a) and (b), but the fitting curves are plotted together. As seen in the figures, the data are well fitted by the Hamiltonian (equation (1)), and from this fitting, we extracted the device parameters, which are listed in table 1 for all the devices. In the table, we also listed the parameters of the device used in [13]. The obtained C_c are quite consistent with the designs.

Next, we investigate the dispersive shift. Using a pulsed readout, we measure Γ as a function of ω_p. By applying a π-pulse to the qubit before the readout, we can measure Γ corresponding to the qubit state $|1\rangle$. The pulse sequence is shown in the inset of figure 3. We use 100 ns long time trace data of the reflected readout pulse, which starts after a delay t_d from the termination of the π-pulse, to extract the amplitude and the phase. The delay t_d is adjusted to give a maximum contrast between the qubit states $|0\rangle$ and $|1\rangle$. Figure 3 shows the amplitude of the normalized reflection coefficient Γ' as a function of ω_p. Γ' is defined as $\Gamma' \equiv (\Gamma - \Gamma_{on})/|\Gamma_{off} - \Gamma_{on}|$, where Γ_{on} and Γ_{off} are the reflection coefficients obtained by the on and the off resonance of the resonator, respectively [13]. For each device, we measure $|\Gamma'|$ with and without the π-pulse, where the qubit is biased at $f = 0.5$. The shifts of the dip frequency correspond to the dispersive shifts. The observed dispersive shifts 2χ and ω_r are summarized in table 2, together with ω_{01} determined by the spectroscopy measurements. In the table, we also listed the theoretical parameters obtained from the energy band calculation using the fitting parameters listed in table 1. The measured dispersive shifts are close to the theoretical predictions which are obtained by calculating the difference between the cavity resonant frequencies when the qubit is in state $|0\rangle$ and state $|1\rangle$. Their magnitudes are much larger than the values estimated under the two-level approximation for the qubit, namely, $|g_{01}^2/\Delta_{01}|$, where $\Delta_{01} = \omega_{01} - \omega_r$. Here, g_{01} represents the matrix element $\langle 1|\mathcal{H}_{cq}^c|0\rangle$, where

Table 1. Parameters of the measured devices.

Device	Designed C_c (fF)	Fitting parameters				
		C_c (fF)	E_J/h (GHz)	E_c/h (GHz)	α	E_r/h (GHz)
A	2	1.86	139	3.55	0.685	10.250
B	3	3.14	146	3.38	0.640	10.252
C	4	4.19	148	3.29	0.613	10.298
[13]	4	4.08	148	3.27	0.611	10.679

Table 2. Magnitude of the dispersive shift. All of the parameters are for the qubit bias $f = 0.5$.

Device	Measured			Theory			
	$\omega_{01}/2\pi$ (GHz)	$\omega_r/2\pi$ (GHz)	$2\chi/2\pi$ (MHz)	$2\chi/2\pi$ (MHz)	$\omega_{01}/2\pi$ (GHz)	$\omega_{12}/2\pi$ (GHz)	$g_{01}/2\pi$ (MHz)
A	3.730	10.236	-13	-10.7	3.727	17.61	76.0
B	4.728	10.232	-37	-35.9	4.725	15.58	143
C	5.350	10.274	-71	-71.8	5.361	14.46	201
[13]	5.504	10.656	-80	-71.5	5.513	14.54	197

$|0\rangle$ and $|1\rangle$ are the ground and the first-excited states of the uncoupled qubit Hamiltonian (equation (2)), respectively, and $\mathcal{H}_{cq}^c$ is the coupling Hamiltonian $\mathcal{H}_c^c$ (equation (4)) restricted onto the qubit subspace. This enhancement is due to the effect of the straddling regime [7]. As seen in table 2, the condition for the straddling regime $\omega_{01} < \omega_r < \omega_{12}$ is satisfied in all the devices.

4. Comparison between the capacitive and the inductive couplings

As shown in the previous section and in [13], we observed a large enhancement of the dispersive shift of the cavity resonance due to the effect of the straddling regime [7]. It was observed in the system shown in figure 4(a), where a flux qubit is coupled to an LC resonator. However, a natural question is why this had not been reported before in much more extensively studied flux-qubit circuits with inductive coupling (figure 4(b)). Since the flux qubits typically have large anharmonicity, satisfying the condition for the straddling regime, namely, $\omega_{01} < \omega_r < \omega_{12}$, is quite easy. In fact, we even unintentionally satisfied this condition in our previous study using inductive coupling, but we did not observe such a large enhancement [17]. The purpose here is to answer this question.

The Hamiltonian of the system where a flux qubit is capacitively coupled to an LC resonator as shown in figure 4(a) is given by

$$\mathcal{H}_C = \mathcal{H}_q^c + \mathcal{H}_r^c + \mathcal{H}_c^c, \tag{1}$$
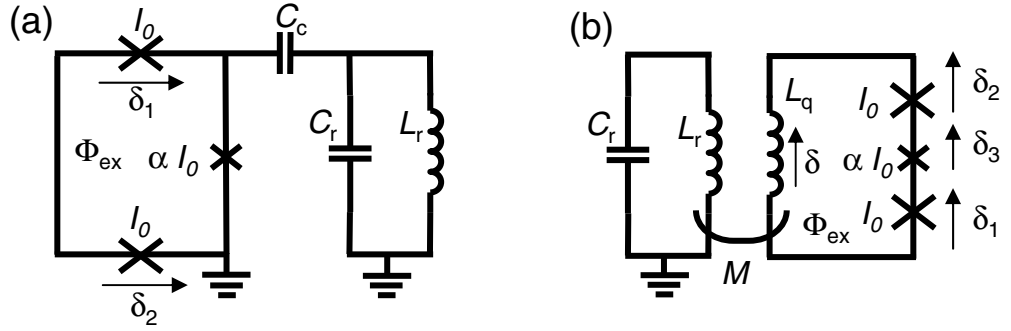
Figure 4. The circuit diagram of (a) a flux qubit capacitively coupled to an LC resonator and (b) a flux qubit inductively coupled to an LC resonator.

which consists of the qubit part, the resonator part and the coupling part. Each term of the Hamiltonian is given as below [13]:

$$\mathcal{H}_q^c = 4 E_c \left[\frac{V}{X}(n_1^2 + n_2^2) + 2\frac{W}{X} n_1 n_2 \right] - E_J \left[\cos\delta_1 - \cos\delta_2 - \alpha\cos(\delta_1 - \delta_2 + 2\pi f) \right], \tag{2}$$

$$\mathcal{H}_r^c = E_r \sqrt{\frac{Y}{X}} \left(a^\dagger a + \frac{1}{2} \right), \tag{3}$$

$$\mathcal{H}_c^c = -2i\frac{\sqrt{\beta_c\gamma}}{Y^{1/4}X^{3/4}}\sqrt{E_r E_c}(n_1 - n_2)(a^\dagger - a), \tag{4}$$

where $E_J = I_0\Phi_0/2\pi$, $f = \Phi_{\text{ex}}/\Phi_0$, $\Phi_0 = h/2e$, $E_c = e^2/2C_J$, $E_r = \hbar/\sqrt{L_r C_r}$, $V = (1 + \alpha)(1 + \gamma) + \beta_c$, $W = \alpha(1 + \gamma) + \beta_c$, $X = (1 + 2\alpha)(1 + \gamma) + 2\beta_c$, $Y = 1 + 2\alpha + 2\beta_c$, $\beta_c = C_c/C_J$ and $\gamma = C_c/C_r$. Here, I_0 and C_J are the critical current and the capacitance of the larger Josephson junction of the qubit, respectively. δ_i and n_i ($i = 1, 2$) are the phase differences across the larger junction, and its conjugate variable representing the charge number, respectively. a ($a^\dagger$) is the annihilation (creation) operator of the photons in the resonator. Finally, L_r and C_r are the equivalent inductance and the capacitance of the resonator, respectively.

Next, we consider the Hamiltonian of the system where a flux qubit is inductively coupled to an LC resonator as shown in figure 4(b). The derivation is given in appendices A and B. The Hamiltonian is given by

$$\mathcal{H}_L = \mathcal{H}_q^l + \mathcal{H}_r^l + \mathcal{H}_c^l, \tag{5}$$

and each term is given as follows:

$$\mathcal{H}_q^l = 2E_c \left(n_a^2 + \frac{1}{1 + 2\alpha}n_s^2 + \frac{2\alpha}{1 + 2\alpha}n_t^2 \right) - E_J[\cos(\delta_a - \delta_s - \delta_t) + \cos(\delta_a + \delta_s + \delta_t)$$

$$+ \alpha\cos(2\pi f - \delta_t/\alpha + 2\delta_s)] + \frac{E_J(1 + 2\alpha)}{2\alpha\beta_L}\delta_t^2, \tag{6}$$

where $\beta_L = \alpha L_q/[(2\alpha + 1)L_J]$, $L_J = \Phi_0/(2\pi I_0)$ and L_q is the loop inductance of the flux qubit. Here, we used the following variable transformations for δ (phase across the loop inductance of

the qubit) and δ_i ($i = 1, 2, 3$ phases across the junction):

$$\delta_t = \frac{-\alpha}{1 + 2\alpha}\delta, \tag{7}$$

$$\delta_s = \frac{1}{2(1 + 2\alpha)}[2\alpha(\delta_3 - 2\pi f) - \delta_1 - \delta_2], \tag{8}$$

$$\delta_a = (\delta_1 - \delta_2)/2, \tag{9}$$

and n_t, n_s and n_a are the corresponding conjugate variables. $\mathcal{H}_r^l$ is given by

$$\mathcal{H}_r^l = E_r\left(a^\dagger a + \frac{1}{2}\right). \tag{10}$$

$\mathcal{H}_c^l$ is given by

$$\mathcal{H}_c^l = -\frac{\pi}{\beta}\frac{E_J}{E_M}\sqrt{E_r E_{Lr}}(\hat{a}^\dagger + \hat{a})\delta_t, \tag{11}$$

where $E_M = \Phi_0^2/(2M)$ and $E_{Lr} = \Phi_0^2/(2L_r)$.

Based on these, we compare the energy band structure of the two systems. Figures 5(a)–(c) show the excitation energy from the ground state, the coupling strength $|g_{ij}|$ and the dispersive shift χ_{ij}, respectively, for the capacitive coupling case. Here, $g_{ij} = \langle i|\mathcal{H}_{cq}^c|j\rangle$, where $|i\rangle$ represents the ith eigenstate of the uncoupled qubit Hamiltonian (equation (2)), and $\chi_{ij} = |g_{ij}|^2/(\omega_{ij} - \omega_r)$, where $\omega_{ij} = \omega_j - \omega_i$. The parameters are taken from device C, namely, $E_J = 148$, $E_c = 3.29$ GHz, $\alpha = 0.613$, $C_c = 4.19$ fF and $\omega_r/2\pi = 10.298$ GHz. Figures 5(d)–(f) show the corresponding calculations for the inductive coupling case. The qubit parameters, E_J, E_c and α, are kept the same as those for the capacitive coupling case. The mutual inductance $M = 8.90$ pH and the resonator frequency $\omega_r = 13.80$ GHz are chosen in such a way that $|g_{01}|$ and $\omega_{01} - \omega_r$, and hence, χ_{01} become almost equal for both of the coupling cases. By comparing figures 5(c) and (f), we see that the total dispersive shift χ_{total} for the inductive coupling case is much smaller than that for the capacitive coupling case. Here, χ_{total} is obtained by calculating $\chi_{01} - \chi_{10} + \sum_{j=2}^{M}(\chi_{j1} - \chi_{1j} - \chi_{j0} + \chi_{0j})/2$ with $M = 4$, and confirmed to be very close to the result obtained by the energy band calculation [13]. χ_{total} at $f = 0.5$ is 8.6 MHz for the inductive coupling, while that for the capacitive coupling is 35.9 MHz. Note that the condition for the straddling regime, $\omega_{01} < \omega_r < \omega_{12}$, is satisfied in both cases. Indeed, the magnitude of χ_{total} is larger than that of χ_{01}, meaning that it is enhanced by the effect of the straddling regime. However, the degree of the enhancement is very different for the two cases.

There are two main reasons that make this difference. Firstly, by comparing figures 5(a) and (c), we see that ω_{12} is much smaller for the capacitive coupling case. Since the qubit parameters are the same, this reduction is due to C_c. This leads to smaller $|\Delta_{12}| = |\omega_r - \omega_{12}|$, and hence larger χ_{12}. Secondly, by comparing figures 5(b) and (e), we see that $|g_{12}|/|g_{01}|$ is larger for the capacitive coupling case. The $|g_{12}|/|g_{01}|$ at $f = 0.50$ is 2.4 for the capacitive coupling, while that for the inductive coupling is 0.77. This also leads to larger χ_{12} in the capacitive coupling case. Thus, we conclude that the capacitive coupling plays an essential role in the observed large enhancement of the dispersive shift.

We can also choose the parameters in such a way that the qubit transition energies (ω_{01} or both ω_{01} and ω_{12}) are similar in the capacitive and the inductive coupling cases. The results are shown in appendix C. The conclusion that $|g_{12}|/|g_{01}|$ and χ_{total} are larger for the capacitive coupling case is the same.
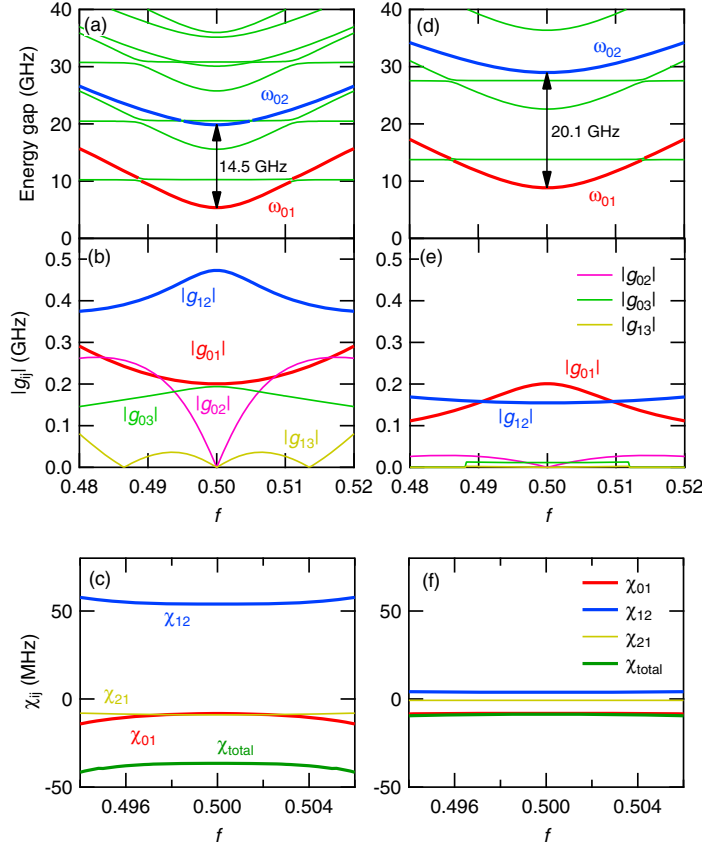
Figure 5. Comparison between the capacitive (a)–(c) and the inductive (d)–(f) couplings. Panels (a) and (d) show the energy gap from the ground state, (b) and (e) show the coupling strength $|g_{ij}| = |\langle i|\mathcal{H}_c|j\rangle|$, and (c) and (f) show the dispersive shift χ_{ij}. For all the figures, $E_J = 148$, $E_c = 3.29\,\text{GHz}$ and $\alpha = 0.613$ are used. For (a)–(c), $C_c = 4.19\,\text{fF}$ and $\omega_r/2\pi = 10.30\,\text{GHz}$ are used. For (d)–(f), $L_q = 50.0\,\text{pH}$, $M = 8.9\,\text{pH}$ and $\omega_r/2\pi = 13.8\,\text{GHz}$ are used.

5. Coherence times

We investigate the coherence properties of the flux qubit capacitively coupled to the resonator. Figure 6 shows an example of the measurements of (a) the energy relaxation and (b) the echo dephasing in device C, where the qubit is biased at $f = 0.5004$. The heterodyne voltage V_0, which is offset in such a way that it becomes zero when the qubit is in the ground state, is plotted as a function of the delay time. The pulse sequence for each measurement is shown in the inset of the figure. The data for the energy relaxation measurement are well fitted by an exponential decay of $\exp(-t/T_1)$ and give the qubit energy relaxation time T_1. The oscillation observed in the echo measurement is due to the fact that the rotation axis of the second $\pi/2$ pulse is rotated at $100\,\text{MHz}$. It is not so clear whether the decay envelope is exponential or Gaussian. In the figure, we fitted the data by an oscillating Gaussian, namely, $\exp(-t/2T_1)\exp[-(t/\tau_{\text{echo}})^2]\sin(\omega t + \phi)$ and extracted the echo decay time τ_{echo}.

We measured the flux bias dependence of T_1 and τ_{echo} in devices B and C, and plot them in figures 7(a) and (c), respectively. T_1 is independent of f in the measured range, and the magnitude is almost the same for both devices in spite of their difference in coupling
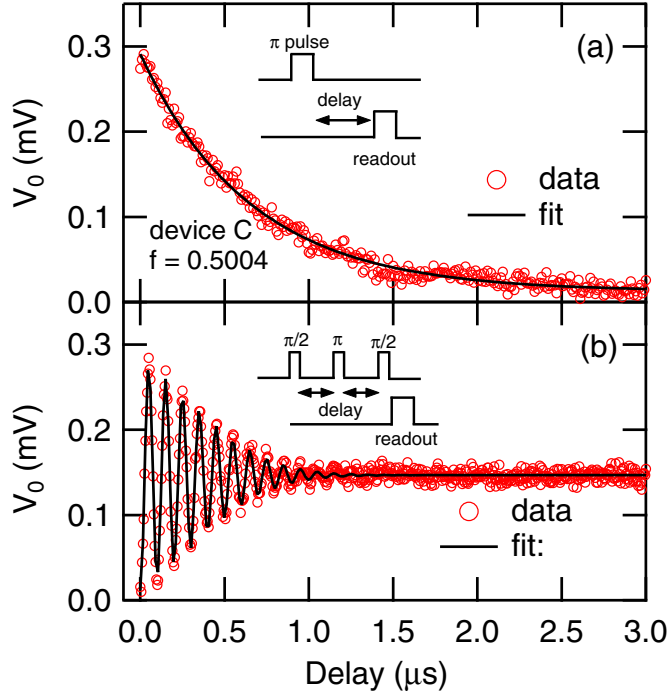
Figure 6. Example of the qubit coherence measurements: (a) energy relaxation and (b) echo decay in device C. The flux qubit is biased at $f = 0.5004$. The heterodyne voltage V_0 is plotted as a function of the delay time in the pulse sequence shown in the inset. The open circles are experimental data and the black curves are the fitting curves.

capacitance. In the figure, we also plot the theoretical predictions based on the Purcell effect, $\kappa(g_{01}/\Delta_{01})^2$ [7]. The observed T_1 are more than one order of magnitude below the Purcell limit, and probably limited by something which commonly exists in both devices, such as the two-level systems at the surface of the substrate [18, 19].

The observed τ_{echo} also looks very similar in the two devices. It becomes maximum at $f = 0.5$ and rapidly decreases as we move away from this bias point. To account for this flux dependence of τ_{echo}, we assumed the dephasing due to the $1/\nu$ flux noise (ν is the frequency), which was carefully studied for the flux-qubit circuit with the dc-SQUID (superconducting quantum interference device) readout [20]. We fitted $1/\tau_{\mathrm{echo}}$ by the derivative of ω_{01} with respect to f, namely,

$$1/\tau_{\mathrm{photon}} = \frac{\sqrt{A \ln 2}}{\hbar} \left| \frac{\partial \omega_{01}}{\partial f} \right|, \tag{12}$$

as shown in figures 7(b) and (d). In both devices, the fitting looks good, and the fitting parameter A is determined to be 6.6×10^{-6} and 6.4×10^{-6} for devices B and C, respectively. These values are of the same order as those reported previously [20–22], supporting the scenario of dephasing due to the $1/\nu$ flux noise.

As shown in the figure, τ_{echo} saturates at $\sim 1\,\mu$s at $f = 0.5$. Note that τ_{echo} is the pure dephasing time and should not be limited by $2T_1$. One possible source of the limit is the dephasing induced by the fluctuations of the photon number in the resonator [1, 23–25]. In the present devices, the cavity decay rate ($\kappa/2\pi = f_{\mathrm{r}}/Q$) is about 15 MHz, and the qubit decay rate ($\gamma/2\pi = T_1^{-1}/2\pi$) is about 230 kHz. Thus, devices B and C are in the strong-dispersive
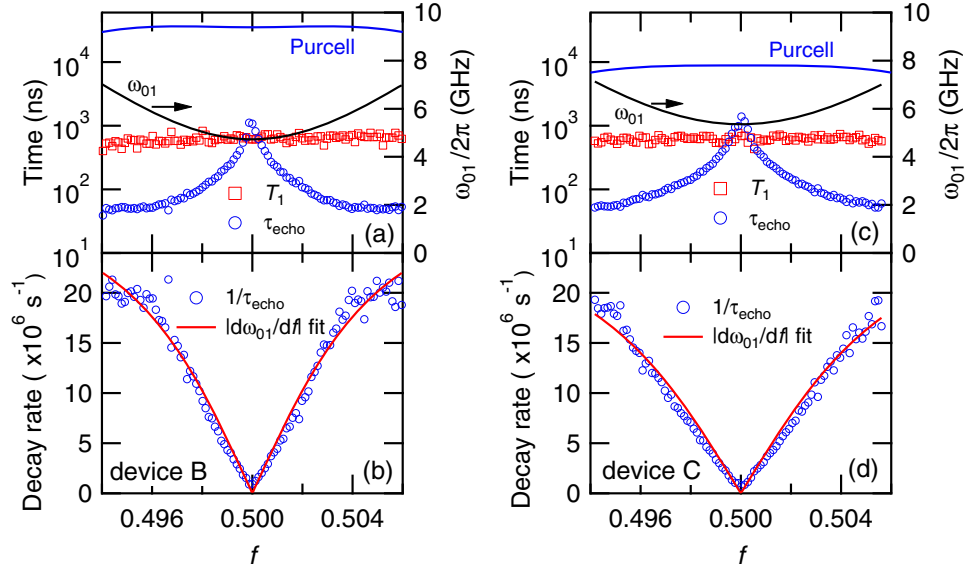
Figure 7. Flux bias dependence of the coherence times. In (a) and (c), the energy relaxation time T_1 and the echo decay time τ_{echo} are plotted as a function of the flux bias f for devices B and C, respectively. In the figures, qubit $|0\rangle$–$|1\rangle$ transition frequency $\omega_{01}/2\pi$ obtained by the spectroscopy measurement is plotted by the black curves. Theoretical prediction for T_1 limited by the single-mode Purcell effect is plotted by the blue curves. In (b) and (d), $1/\tau_{\text{echo}}$ is plotted as a function of f for devices B and C, respectively. The red curves represent the $|\partial\omega_{01}/\partial f|$ fitting.

regime [26], which means that $2\chi > \kappa, \gamma$. As shown in [25], the dephasing rate due to the photon number fluctuations in the strong-dispersive regime is given by

$$\tau_{\text{photon}}^{-1} = \kappa[(\langle n \rangle + 1)N + \langle n \rangle(N + 1)], \tag{13}$$

where $\langle n \rangle$ is the mean photon number in the resonator and N corresponds to the N-photon resonator state. Since the present data were measured using the fundamental qubit transition frequency ($N = 0$),[7] $\tau_{\text{photon}}^{-1}$ is simply given by $\kappa\langle n \rangle$, which does not depend either on χ or f. To account for the τ_{echo} of 1 μs with given κ, $\langle n \rangle$ of 0.01 (or the effective temperature T_{eff} of the resonator of 0.1 K with the assumption that $\langle n \rangle = [\exp(\hbar\omega_{\text{r}}/k_{\text{B}}T_{\text{eff}}) - 1]^{-1}$) is needed, although at present we do not precisely know the actual value of $\langle n \rangle$.

6. Observation of the discrete ac-Stark effect

As shown in the previous section, devices B and C are in the strong-dispersive regime [26]. The hallmark of this regime is the appearance of separate spectral lines of the qubit transition frequency, each of which corresponds to a particular photon number state of the resonator. This effect can be applied to characterize the photon statistics in the resonator [26]. Here, we investigate this effect using device C.

We measured the reflection coefficient Γ of the probe field (frequency $\omega_{\text{p}}/2\pi$ and power P_{p}) applied via the readout port, by varying the frequency $\omega_{\text{d}}/2\pi$ and the power P_{d} of the qubit

---

[7] In the spectroscopy measurement, we observed separate qubit spectral lines corresponding to $N = 0, 1$ and 2 as shown in the next section.
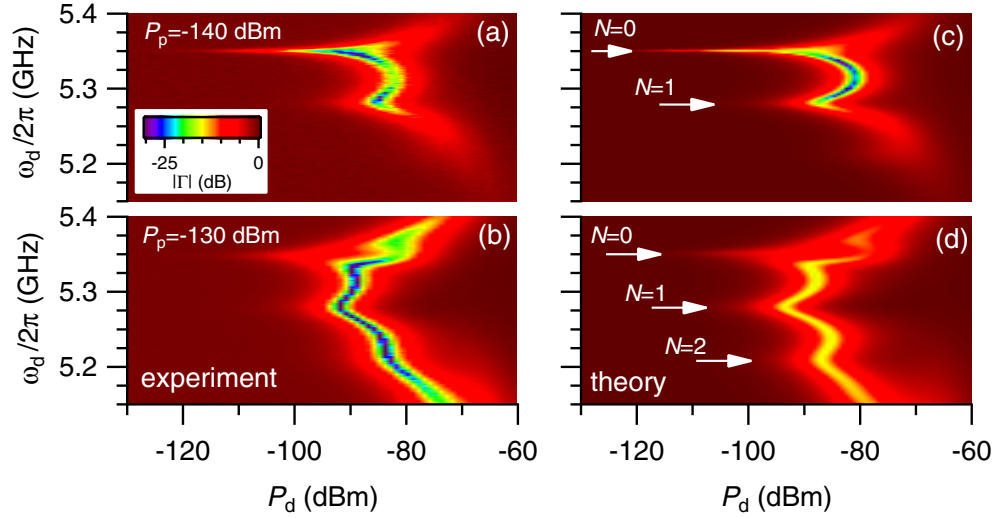
Figure 8. Observation of the discrete ac-Stark effect. The magnitude of the reflection coefficient Γ is plotted as a function of the power P_d and the frequency ω_d of the qubit drive. The frequency of the probe microwave is fixed at $\omega_r/2\pi = 10.274$ GHz, and its power is fixed at (a) -140 dBm and (b) -130 dBm. Panels (c) and (d) are the numerical simulations corresponding to (a) and (b), respectively. The white arrows indicate the qubit frequency when the resonator contains N photons ($N = 0, 1, 2$).

drive field applied via the control port. Figure 8 shows $|\Gamma|$ as a function of P_d and ω_d, where ω_p is fixed at $\omega_r/2\pi = 10.274$ GHz. P_p is -140 dBm for figure 8(a) and -130 dBm for figure 8(b), which correspond to the mean photon number in the resonators of 0.06 and 0.6, respectively. In the strong-dispersive regime, the qubit transition frequency depends on the resonator photon number N as $\omega_{01} - 2N\chi$ ($N = 0, 1, 2, \ldots$), and we expect to observe separate spectral lines at these frequencies. In figure 8(a), we observe a spectral line at $\omega_d/2\pi = 5.350$ GHz at low P_d. This frequency is equal to $\omega_{01}/2\pi$ (see table 2) and corresponds to the zero-photon state. As we increase P_d, another spectral line at 5.279 GHz appears. This frequency is equal to $(\omega_{01} - 2\chi)/2\pi$ and corresponds to the one-photon state. The result of the same measurement with 10 dB higher P_p is shown in figure 8(b). The larger P_p produces the population of higher photon-number states. Indeed, we observe more spectral lines up to the two-photon state.

Note that the observed spectral lines are dips, not peaks. Without the qubit drive, a shallow (< 1 dB) dip is observed at ω_r (data not shown) due to the finite internal quality factor ($\sim 3 \times 10^4$) of the resonator. Thus, a small increase in $|\Gamma|$ is naively expected when the qubit excitation induces the dispersive shift of the cavity resonance, although the expected magnitude of the signal (< 1 dB) is anyway much smaller than that observed here. The origin of these deep dips is inelastic scattering [27], which is intuitively understood as follows.

Figure 9 shows the level structure of the qubit–resonator system in the dispersive regime in a frame rotating at the qubit drive frequency ω_d. Here, we consider only the lowest two levels for the qubit, $|0\rangle_q$ and $|1\rangle_q$: the higher levels do not play an essential role here, except that they enhance the magnitude of the dispersive level shift [13]. Figure 9(a) represents the energy diagram when the qubit drive is turned off. The label for each level $|m, n\rangle$ represents the state where the qubit is in the mth state and the resonator is in the nth state. Note that $|m, n\rangle$ is not a simple product of Fock states of the uncoupled qubit and the resonator due to the coupling g_{ij}.
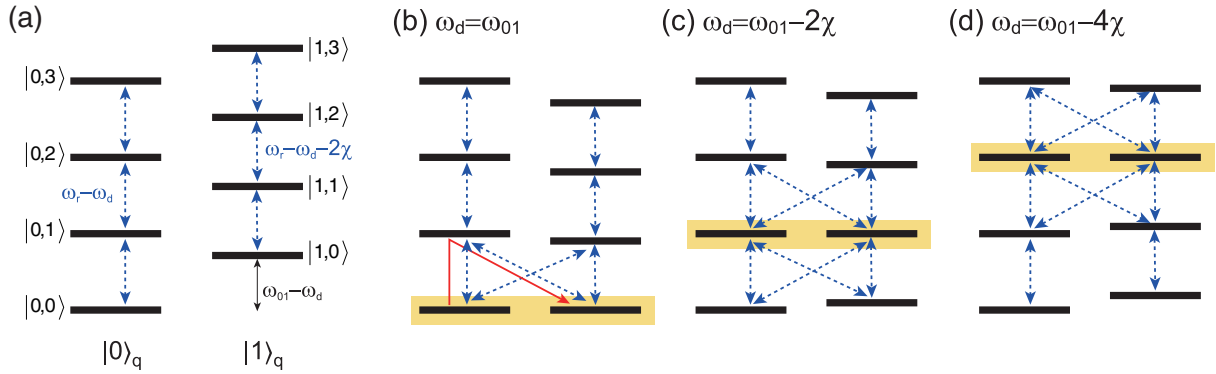
Figure 9. Level structure of the driven qubit–resonator system in the frame rotating at ω_d. The blue arrows indicate the allowed microwave transitions. Since the cavity decay rate is much larger than the qubit decay rate, only the transitions induced by the probe field are indicated. (a) Without driving ($E = 0$). The microwave transitions occur only vertically. (b)–(d) With driving ($E \neq 0$). The drive frequency is tuned at $\omega_d = \omega_{01}$ in (b), $\omega_d = \omega_{01} - 2\chi$ in (c) and $\omega_d = \omega_{01} - 4\chi$ in (d). Oblique transition paths are generated by the mixing induced by the resonant driving of the qubit. Yellow boxes indicate the degenerate two levels, which are mixed strongly by the drive. The red arrow in (b) represents the Raman transition induced by the probe microwave field tuned at ω_r.

However, in the dispersive regime, g_{ij} mixes the two states $|i\rangle_q|n+1\rangle_r$ and $|j\rangle_q|n\rangle_r$ only slightly and produces a dispersive level shift. As a result, the level spacings of the left ladder ($|0\rangle_q$) and the right ladder ($|1\rangle_q$) in figure 9(a) become different. Since there is no qubit drive, the microwave transition is of cavity origin and occurs vertically within each ladder. The probe field, which is adjusted at the transition frequency of the left ladder, is then scattered elastically.

In contrast, when the qubit drive is turned on, state mixing between the two ladders can happen. For example, when $\omega_d = \omega_{01}$, $|0,0\rangle$ and $|1,0\rangle$ become degenerate (figure 9(b), yellow box), and these two states mix strongly. This gives rise to a new radiative decay path from the first excited state of the left ladder (originally $|0,1\rangle$) to the ground state of the right ladder (originally $|1,0\rangle$). Accordingly, the probe field can induce the Raman transition (red arrow in figure 9(b)). This inelastic scattering results in the reduction of the reflection coefficient. We can expect a similar reduction in $|\Gamma|$ when ω_d is adjusted to be $\omega_{01} - 2N\chi$ as shown in figures 9(c) and (d) for $N = 1$ and 2, respectively. As we increase the probe power and accordingly the mean photon number in the resonator, we are able to see the effect for larger N, which is what we observed in figure 8(b).

To understand the experimental results more quantitatively, we analyzed the microwave response of this system using a full-quantum theoretical model in which the qubit, the resonator and the propagating microwave modes are treated quantum mechanically, and calculated the reflection coefficient $|\Gamma|$ (figures 8(c) and (d)) assuming the same parameter values in the experiment. The details of the calculation are summarized in appendix D. We observe fairly good agreement between the experiment and the theory.

7. Conclusion

In conclusion, we studied systematically the system where a superconducting flux qubit is capacitively coupled to an LC resonator. In all three devices with different coupling

capacitances, the dispersive shifts are enhanced by the effect of the straddling regime, which is quantitatively reproduced by the theory. We showed by numerical calculation that the capacitive coupling has two effects on the dispersive shift, namely, to reduce the qubit anharmonicity and to produce the large matrix element g_{12}, both of which lead to the large enhancement in χ. We investigated the coherence properties in these devices. Even in the device with the largest C_c (device C) the observed T_1 is one order below the Purcell limit. We also showed that the flux dependence of the echo dephasing is consistent with the low-frequency flux noise. We also demonstrated the discrete ac-Stark effect using the device in the strong-dispersive regime. The results can be explained by the inelastic scattering of the microwave incident on the resonator, and well reproduced by the numerical calculations.

Acknowledgments

Appendix A. Single flux qubit with non-negligible loop inductance

Here, we derive the Hamiltonian and the central equation for a single flux qubit, where we explicitly take into account the loop inductance. The derivation is based on [28], but with a difference that the periodicity of the potential terms in the Hamiltonian is taken into account. Probably because of this difference, the calculated energy bands do not have the doublet structure reported in [28].

First, we consider a single 3JJ flux qubit with a loop inductance as shown in figure A.1(a). From the flux quantization,

$$\delta_1 + \delta_2 + \delta_3 - \delta = 2\pi f. \tag{A.1}$$

We introduce a dimensionless parameter representing the ratio between the loop inductance and the Josephson inductance

$$\beta_{\mathrm{L}} \equiv \frac{2\pi L_{\mathrm{q}}}{\Phi_0} \left(\frac{1}{I_0} + \frac{1}{I_0} + \frac{1}{\alpha I_0} \right)^{-1} \tag{A.2}$$

$$= \frac{\alpha}{2\alpha + 1} \frac{L_{\mathrm{q}}}{L_{\mathrm{J}}}, \tag{A.3}$$

where

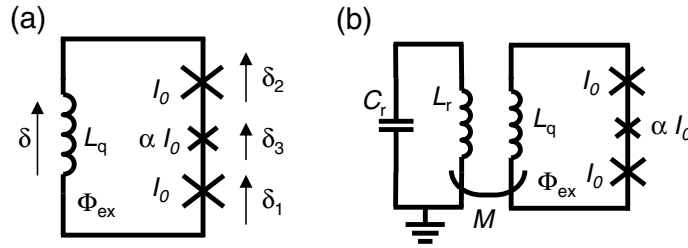$$L_{\mathrm{J}} \equiv \frac{\Phi_0}{2\pi} \frac{1}{I_0}. \tag{A.4}$$

Figure A.1. The circuit diagram of (a) a single 3JJ flux qubit with non-negligible loop inductance and (b) a flux qubit inductively coupled to an LC resonator.

Following [28], we perform the following variable transformations:

$$\delta_{\mathrm{t}} = \frac{-\alpha}{1 + 2\alpha} \delta, \tag{A.5}$$

$$\delta_{\mathrm{s}} = \frac{1}{2(1 + 2\alpha)} [2\alpha(\delta_3 - 2\pi f) - \delta_1 - \delta_2], \tag{A.6}$$

$$\delta_{\mathrm{a}} = (\delta_1 - \delta_2)/2, \tag{A.7}$$

or equivalently

$$\delta_1 = \delta_{\mathrm{a}} - \delta_{\mathrm{t}} - \delta_{\mathrm{s}}, \tag{A.8}$$

$$\delta_2 = -(\delta_{\mathrm{a}} + \delta_{\mathrm{t}} + \delta_{\mathrm{s}}), \tag{A.9}$$

$$\delta_3 = 2\pi f - \delta_{\mathrm{t}}/\alpha + 2\delta_{\mathrm{s}}. \tag{A.10}$$

The potential energy of the JJs is expressed by

$$U_{\mathrm{J}} = -E_{\mathrm{J}}[\cos(\delta_{\mathrm{a}} - \delta_{\mathrm{s}} - \delta_{\mathrm{t}}) + \cos(\delta_{\mathrm{a}} + \delta_{\mathrm{s}} + \delta_{\mathrm{t}}) + \alpha \cos(2\pi f - \delta_{\mathrm{t}}/\alpha + 2\delta_{\mathrm{s}})] \tag{A.11}$$

$$= -\frac{E_{\mathrm{J}}}{2}\left[\mathrm{e}^{\mathrm{i}(\delta_{\mathrm{a}}+\delta_{\mathrm{s}})}\mathrm{e}^{\mathrm{i}\delta_{\mathrm{t}}} + \mathrm{e}^{-\mathrm{i}(\delta_{\mathrm{a}}-\delta_{\mathrm{s}})}\mathrm{e}^{\mathrm{i}\delta_{\mathrm{t}}} + \mathrm{e}^{\mathrm{i}(\delta_{\mathrm{a}}-\delta_{\mathrm{s}})}\mathrm{e}^{-\mathrm{i}\delta_{\mathrm{t}}} + \mathrm{e}^{-\mathrm{i}(\delta_{\mathrm{a}}+\delta_{\mathrm{s}})}\mathrm{e}^{-\mathrm{i}\delta_{\mathrm{t}}}\right]$$

$$- \alpha\frac{E_{\mathrm{J}}}{2}\left[\mathrm{e}^{\mathrm{i}2\delta_{\mathrm{s}}}\mathrm{e}^{\mathrm{i}(2\pi f - \delta_{\mathrm{t}}/\alpha)} + \mathrm{e}^{-\mathrm{i}2\delta_{\mathrm{s}}}\mathrm{e}^{-\mathrm{i}(2\pi f - \delta_{\mathrm{t}}/\alpha)}\right], \tag{A.12}$$

where $E_{\mathrm{J}} = \Phi_0 I_0/(2\pi)$. The energy of the loop inductance is

$$U_{\mathrm{l}} = \frac{1}{2L_{\mathrm{q}}}\left(\frac{\Phi_0}{2\pi}\right)^2 \delta^2 \tag{A.13}$$

$$= \frac{E_{\mathrm{J}}(1 + 2\alpha)}{2\alpha\beta_L} \delta_{\mathrm{t}}^2. \tag{A.14}$$

The kinetic energy of the JJs is

$$T = \frac{C_{\mathrm{J}}}{2}\left(\frac{\Phi_0}{2\pi}\right)^2 [\dot{\delta_1}^2 + \dot{\delta_2}^2 + \alpha\dot{\delta_3}^2], \tag{A.15}$$

where C_{J} is the capacitance of the larger JJ. Using equations (A.8) and (A.10)

$$T = \frac{C_{\mathrm{J}}}{2}\left(\frac{\Phi_0}{2\pi}\right)^2 \left[2\dot{\delta_{\mathrm{a}}}^2 + 2(1 + 2\alpha)\dot{\delta_{\mathrm{s}}}^2 + \frac{1 + 2\alpha}{\alpha}\dot{\delta_{\mathrm{t}}}^2\right]. \tag{A.16}$$

Note that there are no cross terms such as $\dot{\delta}_a\dot{\delta}_s$ thanks to the variable transformation. The Lagrangian of the system is

$$\mathcal{L}_q = T - U_J - U_l \tag{A.17}$$

and the canonical momentum is

$$p_i = \frac{\partial \mathcal{L}_q}{\partial \dot{\delta}_i}, \tag{A.18}$$

where $i = a, s$ and t. Finally, the Hamiltonian is given by

$$\mathcal{H}_q = \sum_i p_i \dot{\delta}_i - \mathcal{L}_q \tag{A.19}$$

$$= \frac{2E_c}{\hbar^2}\left(p_a^2 + \frac{1}{1+2\alpha}p_s^2 + \frac{2\alpha}{1+2\alpha}p_t^2\right) + U_J + U_l, \tag{A.20}$$

where E_c is defined for a single charge, namely $E_c = e^2/(2C_J)$. This Hamiltonian can be regarded as a 3JJ flux qubit without the loop inductance interacting with a harmonic oscillator. The harmonic oscillator part (third and fifth terms in equation(A.20)) can be transformed as

$$\frac{2E_c}{\hbar^2}\frac{2\alpha}{1+2\alpha}p_t^2 + \frac{E_J(1+2\alpha)}{2\alpha\beta_L}\delta_t^2 = \frac{p_t^2}{2m_t} + \frac{1}{2}m_t\omega_t^2\delta_t^2, \tag{A.21}$$

$$m_t = \frac{\hbar^2}{8E_c}\frac{1+2\alpha}{\alpha}, \tag{A.22}$$

$$\omega_t = \frac{2E_c}{\hbar}\sqrt{\frac{2E_J}{\beta_L E_c}}. \tag{A.23}$$

As in [28], we choose for our basis functions the product states

$$|\phi_{klm}\rangle = |\phi_k^a\rangle|\phi_l^s\rangle|\phi_m^t\rangle, \tag{A.24}$$

where the first two states are plane waves

$$|\phi_k^a\rangle = (2\pi)^{-1/2}e^{-ik\delta_a}, \tag{A.25}$$

$$|\phi_l^s\rangle = (2\pi)^{-1/2}e^{-il\delta_s} \tag{A.26}$$

and the third state is a harmonic oscillator wave function in δ_t

$$|\phi_m^t\rangle = \left[\frac{m_t\omega_t}{2^{2m}\pi\hbar(m!)^2}\right]^{1/4} H_m\left[\sqrt{\frac{m_t\omega_t}{\hbar}}\delta_t\right]\exp\left[\frac{-m_t\omega_t\delta_t^2}{2\hbar}\right], \tag{A.27}$$

where $H_m[\delta]$ is the mth Hermite polynomial. The wavefunction of the Hamiltonian is given by

$$|\phi\rangle = \sum_{(k,l)\in\vec{g}}\sum_m C(k,l,m)|\phi_{klm}\rangle, \tag{A.28}$$

where the first sum of k and l is taken for the reciprocal lattice of $U_J(k,l)$ [29]. The qubit potential energy has the following translational symmetry with respect to δ_a and δ_s
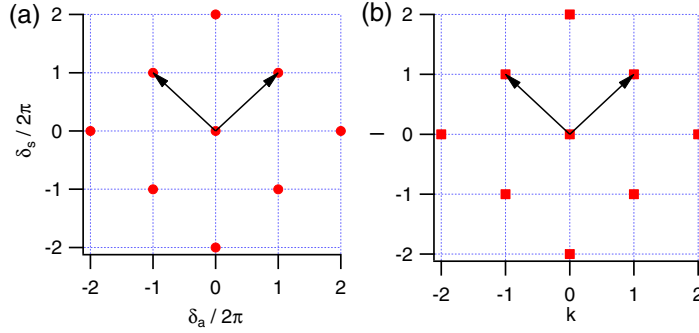
$$\delta_a \rightarrow \delta_a + 2\pi, \tag{A.29}$$

Figure A.2. (a) Real space lattice of U_J and (b) the reciprocal lattice. The arrows represent the unit vectors.

$$\delta_s \to \delta_s + 2\pi, \tag{A.30}$$

$$\delta_a, \ \delta_s \to \delta_a + \pi, \ \delta_s + \pi. \tag{A.31}$$

Thus, its symmetry forms a two-dimensional face-centered lattice as shown in figure A.2(a). It is not a simple square lattice, which is due to the variable transformation. The corresponding reciprocal lattice is also a face-centered lattice shown in figure A.2(b). Thus, the sum for (k, l) in equation (A.28) must be taken for this lattice, and how many points we should take depends on what accuracy we need. Using $p_i = -i\hbar \frac{\partial}{\partial \delta_i}$, the Schrödinger equation $\mathcal{H}|\phi_{klm}\rangle = \epsilon|\phi_{klm}\rangle$ is written as

$$\sum{}' \left[2E_c k^2 + \frac{2E_c}{1+2\alpha} l^2 + m\hbar\omega_t \right] C(k, l, m)|\phi_{klm}\rangle - \sum{}' U_J C(k, l, m)|\phi_{klm}\rangle$$

$$= \epsilon \sum{}' C(k, l, m)|\phi_{klm}\rangle, \tag{A.32}$$

where $\sum'$ means $\sum_{(k,l)\in\vec{g}} \sum_m$. By multiplying $\langle\phi_{k'l'm'}|$ on both sides, we obtain the following central equation:

$$\left[2E_c k'^2 + \frac{2E_c}{1+2\alpha} l'^2 + m'\hbar\omega_t \right] C(k', l', m') - \frac{E_J}{2} \sum_m \left[C(k'-1, l'-1, m)\langle\phi_{m'}^t|e^{i\delta_t}|\phi_m^t\rangle \right.$$

$$+ C(k'+1, l'-1, m)\langle\phi_{m'}^t|e^{i\delta_t}|\phi_m^t\rangle + C(k'-1, l'+1, m)\langle\phi_{m'}^t|e^{-i\delta_t}|\phi_m^t\rangle$$

$$+ C(k'+1, l'+1, m)\langle\phi_{m'}^t|e^{-i\delta_t}|\phi_m^t\rangle \Big] - \alpha\frac{E_J}{2} \sum_m \Big[C(k', l'-2, m)e^{i2\pi f}$$

$$\times \langle\phi_{m'}^t|e^{-i\delta_t/\alpha}|\phi_m^t\rangle + C(k', l'+2, m)e^{-i2\pi f}\langle\phi_{m'}^t|e^{i\delta_t/\alpha}|\phi_m^t\rangle \Big] = \epsilon C(k', l', m'). \tag{A.33}$$

To solve the above equation, we use the following formula [30]:

$$\langle n|e^{c\hat{x}}|m\rangle = (m!n!)^{-1/2} e^{\frac{\hbar c^2}{4m_t\omega_t}} \sum_{j=0}^{\min(m,n)} j! \binom{m}{j} \binom{n}{j} \left(\frac{\hbar}{2m_t\omega_t}\right)^{(m+n-2j)/2} c^{m+n-2j}, \tag{A.34}$$

where $|m\rangle$ is the mth eigenfunction of the harmonic oscillator and c is a constant which can be a complex number. For example, to calculate $\langle\phi_{m'}^{\mathrm{t}}|e^{i\delta_{\mathrm{t}}}|\phi_m^{\mathrm{t}}\rangle$, we use the above formula with

$$c = i \tag{A.35}$$

$$\frac{\hbar}{2m_{\mathrm{t}}\omega_{\mathrm{t}}} = \frac{2\alpha}{1+2\alpha}\sqrt{\frac{\beta_L E_{\mathrm{c}}}{2E_{\mathrm{J}}}}. \tag{A.36}$$

By numerically solving the central equation (A.33) for (k', l') in the subset of the reciprocal lattice and m' from 0 to a certain number, we obtain the energy band diagram for a flux qubit with non-negligible loop inductance.

Appendix B. Flux qubit inductively coupled to an LC resonator

Next, we consider a flux qubit inductively coupled to an LC resonator as shown in figure 1(b). The Hamiltonian consists of three parts, namely,

$$\mathcal{H}_L = \mathcal{H}_{\mathrm{q}}^l + \mathcal{H}_{\mathrm{r}}^l + \mathcal{H}_{\mathrm{c}}^l. \tag{B.1}$$

$\mathcal{H}_{\mathrm{q}}^l$ is already shown in equation (A.20). $\mathcal{H}_{\mathrm{r}}^l$ is simply given by

$$\mathcal{H}_{\mathrm{r}}^l = E_{\mathrm{r}}\left(a^\dagger a + \frac{1}{2}\right), \tag{B.2}$$

where $E_{\mathrm{r}} = \hbar/\sqrt{L_{\mathrm{r}}C_{\mathrm{r}}}$, and a ($a^\dagger$) is the annihilation (creation) operator of the photons in the resonator. $\mathcal{H}_{\mathrm{c}}^l$ is given by

$$\mathcal{H}_{\mathrm{c}}^l = \frac{M}{L_{\mathrm{r}}L_{\mathrm{q}}}\left(\frac{\Phi_0}{2\pi}\right)^2\delta_{\mathrm{r}}\delta. \tag{B.3}$$

Using equations (A.3), (A.5) and

$$\frac{\delta_{\mathrm{r}}}{L_{\mathrm{r}}} = \left(\frac{2\pi}{\Phi_0}\right)\sqrt{\frac{E_{\mathrm{r}}}{2L_{\mathrm{r}}}}(\hat{a}^\dagger + \hat{a}), \tag{B.4}$$

we obtain

$$\mathcal{H}_{\mathrm{c}}^l = -M\frac{E_{\mathrm{J}}}{\beta_L}\left(\frac{2\pi}{\Phi_0}\right)\sqrt{\frac{E_{\mathrm{r}}}{2L_{\mathrm{r}}}}(\hat{a}^\dagger + \hat{a})\delta_{\mathrm{t}} \tag{B.5}$$

$$= -\frac{\pi}{\beta_L}\frac{E_{\mathrm{J}}}{E_M}\sqrt{E_{\mathrm{r}}E_{L\mathrm{r}}}(\hat{a}^\dagger + \hat{a})\delta_{\mathrm{t}}, \tag{B.6}$$

where we defined

$$E_M \equiv \frac{\Phi_0^2}{2M}, \tag{B.7}$$

$$E_{L\mathrm{r}} \equiv \frac{\Phi_0^2}{2L_{\mathrm{r}}}. \tag{B.8}$$

The matrix elements $\langle\phi_{klm}|\delta_{\mathrm{t}}|\phi_{k'l'm'}\rangle$ are given by

$$\langle\phi_{klm}|\delta_{\mathrm{t}}|\phi_{k'l'm'}\rangle = \delta_{k,k'}\delta_{l,l'}\langle\phi_m^t|\delta_{\mathrm{t}}|\phi_{m'}^t\rangle. \tag{B.9}$$
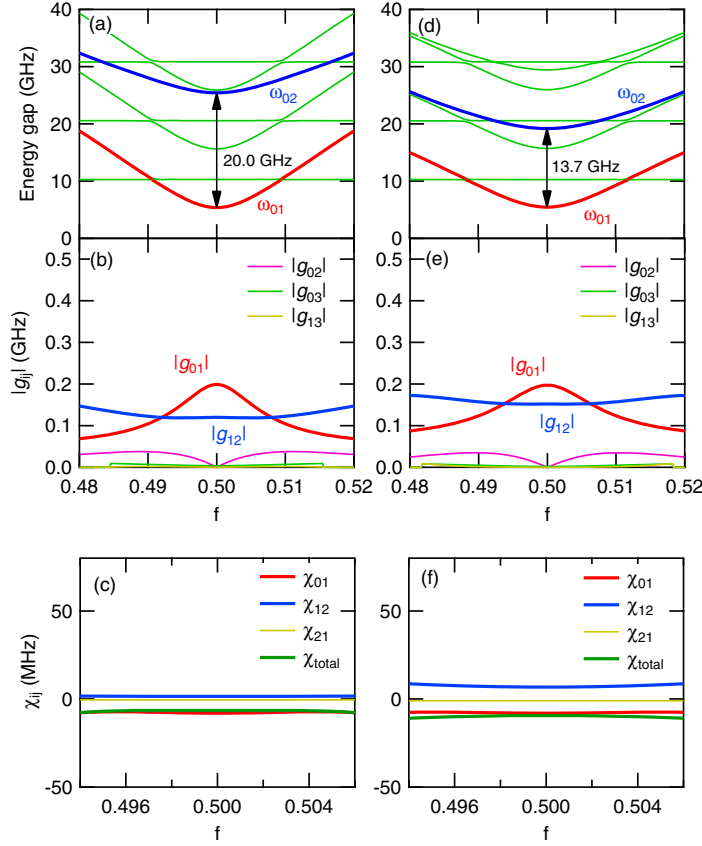
Figure C.1. Numerical calculations for the inductively coupled system of the qubit and the resonator. Panels (a) and (d) show the energy gap from the ground state, (b) and (e) show the coupling strength $|g_{ij}| = |\langle i|\mathcal{H}_c|j\rangle|$ and (c) and (f) show the dispersive shift χ_{ij}. For (a)–(c), $E_J = 148$, $E_c = 3.29\,\text{GHz}$, $\alpha = 0.671$, $L_q = 50.0$, $M = 10.2\,\text{pH}$ and $\omega_r/2\pi = 10.3\,\text{GHz}$ are used. For (d)–(f), $E_J = 148$, $E_c = 1.80\,\text{GHz}$, $\alpha = 0.602$, $L_q = 50.0$, $M = 12.0\,\text{pH}$ and $\omega_r/2\pi = 10.3\,\text{GHz}$ are used.

And the last term is given by

$$\langle \phi_m^t | \delta_t | \phi_{m'}^t \rangle = \begin{cases} \sqrt{m'+1}\sqrt{\frac{2\alpha}{1+2\alpha}}\left(\frac{\beta_L E_c}{2E_J}\right)^{1/4} & (m = m'+1), \\ \sqrt{m'}\sqrt{\frac{2\alpha}{1+2\alpha}}\left(\frac{\beta_L E_c}{2E_J}\right)^{1/4} & (m = m'-1), \\ 0 & (m \neq m' \pm 1). \end{cases} \tag{B.10}$$

In the calculation of figure 5(d), 121 reciprocal lattice points are used for k and l, while m is taken from 0 to 2. The number of bases used for the resonator state is 5.

Appendix C. Numerical calculation with different parameters

In this appendix, we show the results of the numerical calculation for the inductively coupled system of the qubit and the resonator, but with different parameters from those used in figure 5. Figures C.1(a)–(c) show the flux bias dependence of the excitation energy from the ground state, the coupling strength $|g_{ij}|$ and the dispersive shift χ_{ij}, respectively. Here, we adjusted the
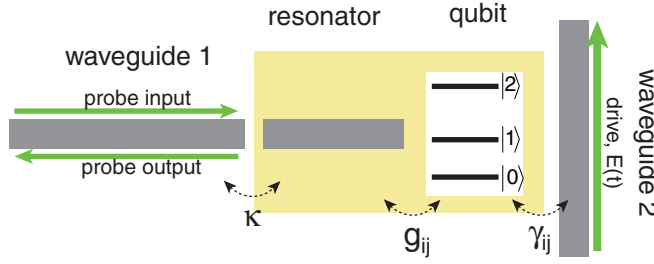
Figure D.1. Theoretical model. A qubit is coupled dispersively to a resonator, which is further coupled to the readout line (waveguide 1). The qubit is driven by a microwave field propagating along the qubit control line (waveguide 2).

qubit parameter α in such a way that ω_{01} is almost equal to that for the capacitive coupling case (figures 5(a)). Also, the mutual inductance M is adjusted so that $|g_{01}|$ becomes almost equal to that for the capacitive coupling case (figure 5(b)). Similar to the results shown in figures 5(e) and (f), $|g_{12}|/|g_{01}|$ and χ_{total} are much smaller than those for the capacitive coupling case. We can also adjust the qubit parameters (E_{c} and α) such that both ω_{01} and ω_{12} are similar to those for the capacitive coupling case. As shown in figures C.1(d)–(f), the overall behavior is the same, which indicates that the smaller $|g_{12}|/|g_{01}|$ is not due to the larger anharmonicity.

Appendix D. Theory of microwave response of the qubit–resonator system

In this appendix, we analyze the microwave response of the present qubit–resonator system. Figure D.1 is a schematic of the theoretical model, which consists of a superconducting qubit, a resonator and waveguides. The lowest two levels of the qubit ($|0\rangle$ and $|1\rangle$) are relevant here in essence. However, to account for the dispersive level shift due to the second excited state $|2\rangle$ [13], we incorporate this level in our model. We refer to the readout line coupled to the resonator as waveguide 1, and the qubit control line as waveguide 2. We apply a monochromatic field $E(t) = E\mathrm{e}^{-\mathrm{i}\omega_{\text{d}}t}$ to drive the qubit through waveguide 2. By defining v as the microwave velocity in the waveguides, the Hamiltonian of the system is

$$\mathcal{H}(t) = \mathcal{H}_{\text{sys}}(t) + \mathcal{H}_{\text{damp}}, \tag{D.1}$$

$$\mathcal{H}_{\text{sys}}(t)/\hbar = \sum_j \bar{\omega}_j \sigma_{jj} + \bar{\omega}_{\text{r}} a^\dagger a + \sum_{i,j} g_{ij}(\sigma_{ji}a + a^\dagger \sigma_{ij}) + \sum_{i,j} \sqrt{\gamma_{ij}}[E(t)\sigma_{ji} + E^*(t)\sigma_{ij}], \tag{D.2}$$

$$\mathcal{H}_{\text{damp}}/\hbar = \int \mathrm{d}k \left[vk b_k^\dagger b_k + \sqrt{v\kappa/2\pi}(a^\dagger b_k + b_k^\dagger a) \right]$$

$$+ \int \mathrm{d}k \left[vk c_k^\dagger c_k + \sum_{i,j} \sqrt{v\gamma_{ij}/2\pi}(\sigma_{ji}c_k + c_k^\dagger \sigma_{ij}) \right], \tag{D.3}$$

where $\sigma_{ij} = |i\rangle\langle j|$ is the transition operator of the qubit, a is the annihilation operator of the resonator and b_k (c_k) is the annihilation operator of the photon propagating in waveguide 1 (2) with wavenumber k. $\bar{\omega}_j$ is the *bare* eigenenergy of the jth qubit level with $\bar{\omega}_0 = 0$ (the eigenenergy of $\mathcal{H}_{\text{q}}^{\text{c}}$, equation (2)), $\bar{\omega}_{\text{r}}$ is the *bare* resonator frequency ($\hbar\bar{\omega}_{\text{r}} = E_{\text{r}}\sqrt{Y/X}$ (see equation (3))), g_{ij} is the qubit–resonator coupling, κ is the resonator decay rate and γ_{ij} is the

qubit decay rate for the $|j\rangle \rightarrow |i\rangle$ transition. From the parity selection rule and the rotating-wave approximation, g_{ij} and γ_{ij} are non-zero only for $(i, j) = (0, 1)$ and $(1, 2)$.

By switching to a frame rotating at the drive frequency ω_{d}, the Hamiltonian becomes static. $\mathcal{H}_{\mathrm{sys}}$ is then given by

$$\mathcal{H}_{\mathrm{sys}}/\hbar = \sum_j (\bar{\omega}_j - j\omega_{\mathrm{d}})\sigma_{jj} + (\bar{\omega}_{\mathrm{r}} - \omega_{\mathrm{d}})a^\dagger a + \sum_{i,j} \left[g_{ij}(\sigma_{ji}a + a^\dagger \sigma_{ij}) + \sqrt{\gamma_{ij}}(E\sigma_{ij} + E^*\sigma_{ij}) \right]. \tag{D.4}$$

$\mathcal{H}_{\mathrm{damp}}$ remains unchanged except that the photon frequency is measured from ω_{d}. We define the dressed states of the qubit–resonator system as the eigenstates of $\mathcal{H}_{\mathrm{sys}}$. We denote them by $|\tilde{j}\rangle$ and their energies by $\tilde{\omega}_j$ ($j = 1, 2, \dots$) from the lowest. $|\tilde{j}\rangle$ corresponds to the states shown in figures 9(b)–(d), or the states in figure 9(a) if $E = 0$. In the dressed-state basis, the Hamiltonian of the overall system is rewritten as

$$\mathcal{H} = \mathcal{H}_{\mathrm{sys}} + \mathcal{H}_{\mathrm{damp}}, \tag{D.5}$$

$$\mathcal{H}_{\mathrm{sys}}/\hbar = \sum_j \tilde{\omega}_j \tilde{\sigma}_{jj}, \tag{D.6}$$

$$\mathcal{H}_{\mathrm{damp}}/\hbar = \int \mathrm{d}k \left[vk b_k^\dagger b_k + \sum_{i,j} \sqrt{v\tilde{\kappa}_{ij}/2\pi}(\tilde{\sigma}_{ij}b_k + b_k^\dagger \tilde{\sigma}_{ji}) \right]$$
$$+ \int \mathrm{d}k \left[vk c_k^\dagger c_k + \sum_{i,j} \sqrt{v\tilde{\gamma}_{ij}/2\pi}(\tilde{\sigma}_{ij}c_k + c_k^\dagger \tilde{\sigma}_{ji}) \right], \tag{D.7}$$

where $\tilde{\sigma}_{ij} = |\tilde{i}\rangle\langle\tilde{j}|$, $\tilde{\kappa}_{ij}$ ($\tilde{\gamma}_{ij}$) is the radiative decay rate into waveguide 1 (2) for the $|\tilde{j}\rangle \rightarrow |\tilde{i}\rangle$ transition. They are, respectively, given by

$$\tilde{\kappa}_{ij} = \kappa |\langle \tilde{j}|a^\dagger|\tilde{i}\rangle|^2, \tag{D.8}$$

$$\tilde{\gamma}_{ij} = \left| \sum_{m,n} \sqrt{\gamma_{mn}} \langle \tilde{j}|\sigma_{mn}|\tilde{i}\rangle \right|^2. \tag{D.9}$$

We work in the dressed-state basis to analyze the microwave response of the system to a probe field applied from waveguide 1. From equation (D.5), the Heisenberg equation for $\tilde{\sigma}_{ij}$ is

$$\frac{\mathrm{d}}{\mathrm{d}t}\tilde{\sigma}_{ij} = \sum_{m,n} \left[\eta_{ijmn}\tilde{\sigma}_{mn} + \xi_{ijmn}^\kappa \tilde{\sigma}_{mn}b_{\mathrm{in}}(t) + \xi_{jinm}^\kappa b_{\mathrm{in}}^\dagger(t)\tilde{\sigma}_{mn} + \xi_{ijmn}^\gamma \tilde{\sigma}_{mn}c_{\mathrm{in}}(t) + \xi_{jinm}^\gamma c_{\mathrm{in}}^\dagger(t)\tilde{\sigma}_{mn} \right], \tag{D.10}$$

where b_{in} (c_{in}) is the input field operator for waveguide 1 (2). By denoting $S_\mu = \sum_{i,j} \sqrt{\tilde{\mu}_{ij}}\tilde{\sigma}_{ji}$ ($\mu = \kappa, \gamma$), the coefficients η_{ijmn} and ξ_{ijmn}^μ are given by

$$\eta_{ijmn} = \mathrm{i}(\tilde{\omega}_i - \tilde{\omega}_j)\delta_{im}\delta_{jn} - \sum_{\mu=\kappa,\gamma} \langle \tilde{m}|[\tilde{\sigma}_{ij}, S_\mu^\dagger]S_\mu + S_\mu^\dagger[S_\mu, \tilde{\sigma}_{ij}]|\tilde{n}\rangle/2, \tag{D.11}$$

$$\xi_{ijmn}^\mu = \mathrm{i}\sqrt{v}\langle \tilde{m}|[S_\mu^\dagger, \tilde{\sigma}_{ij}]|\tilde{n}\rangle. \tag{D.12}$$

We apply a probe field with amplitude F and frequency ω_{p} from waveguide 1, while we apply no probe field from waveguide 2. Therefore, $\langle b_{\mathrm{in}}(t)\rangle = F e^{-\mathrm{i}(\omega_{\mathrm{p}}-\omega_{\mathrm{d}})t}$ and $\langle c_{\mathrm{in}}(t)\rangle = 0$. Note that

the probe frequency ω_p is measured from the drive frequency ω_d in the rotating frame. The stationary solution of the equation (D.10) is then written as

$$\langle \tilde{\sigma}_{ij} \rangle = \sum_{m=0,\pm 1,\dots} A_{ij}^m e^{im(\omega_p - \omega_d)t}.$$ (D.13)

Substituting equation (D.13) into equation (D.10) and solving the linear simultaneous equations together with the condition that $\text{Tr}(\tilde{\sigma}) = 1$, i.e. $\sum_j A_{jj}^m = \delta_{m0}$, we numerically determine A_{ij}^m. Reliable numerical results are obtained by setting $-2 \leqslant m \leqslant 2$ and $1 \leqslant i, j \leqslant 8$. The output field amplitude $\langle b_{out}(t) \rangle$ for waveguide 1 is related to the input one by $\langle b_{out}(t) \rangle = \langle b_{in}(t) \rangle - i\langle S_\kappa(t) \rangle$. The reflected field contains high-order harmonics due to the nonlinear effect. However, in the reflectivity measurement, only the field at the fundamental frequency ($m = -1$) is relevant. The reflection coefficient is defined by $\Gamma = \langle b_{out}(t) \rangle^{m=-1}/\langle b_{in}(t) \rangle^{m=-1}$. Therefore,

$$\Gamma = 1 - i \sum_{i,j} \sqrt{\tilde{\kappa}_{ij}} A_{ji}^{-1}/F.$$ (D.14)

In the numerical simulation, we have chosen the bare parameters of the qubit–cavity system ($\bar{\omega}_1$, $\bar{\omega}_2$, g_{01} and g_{12}) to reproduce the following experimentally measured parameters, $\omega_{01}/2\pi = 5.35\,\text{GHz}$, $\omega_r/2\pi = 10.27\,\text{GHz}$ and $2\chi/2\pi = 71\,\text{MHz}$. We have set $\kappa/2\pi = 15\,\text{MHz}$ as stated in the main text. We employed the qubit radiative decay rate into waveguide 2 as γ_{10}, which is estimated to be $\gamma_{10}/2\pi = 88\,\text{Hz}$ from the Rabi oscillation measurement. We determined F based on the experimental parameter P_p. γ_{21} has almost no effect on the numerical results.

References

[1] Blais A, Huang R S, Wallraff A, Girvin S M and Schoelkopf R J 2004 *Phys. Rev.* A **69** 062320
[2] Wallraff A, Schuster D I, Blais A, Frunzio L, Huang R S, Majer J, Kumar S, Girvin S M and Schoelkopf R J 2004 *Nature* **431** 162
[3] Siddiqi I, Vijay R, Metcalfe M, Boaknin E, Frunzio L, Schoelkopf R J and Devoret M H 2006 *Phys. Rev.* B **73** 054510
[4] Devoret M, Girvin S and Schoelkopf R 2007 *Ann. Phys.* **16** 767
[5] Steffen M, Kumar S, DiVincenzo D, Keefe G, Ketchen M, Rothwell M B and Rozen J 2010 *Appl. Phys. Lett.* **96** 102506
[6] Wirth T, Lisenfeld J, Lukashenko A and Ustinov A V 2010 *Appl. Phys. Lett.* **97** 262508
[7] Koch J, Yu T M, Gambetta J, Houck A A, Schuster D I, Majer J, Blais A, Devoret M H, Girvin S M and Schoelkopf R J 2007 *Phys. Rev.* A **76** 042319
[8] Sillanpää M A, Park J I and Simmonds R W 2007 *Nature* **449** 438
[9] Lupaşcu A, Verwijs C J M, Schouten R N, Harmans C J P M and Mooij J E 2004 *Phys. Rev. Lett.* **93** 177006
[10] Abdumalikov A A, Astafiev O, Nakamura Y, Pashkin Y A and Tsai J 2008 *Phys. Rev.* B **78** 180502
[11] Steffen M, Kumar S, DiVincenzo D P, Rozen J R, Keefe G A, Rothwell M B and Ketchen M B 2010 *Phys. Rev. Lett.* **105** 100502
[12] You J Q, Hu X, Ashhab S and Nori F 2007 *Phys. Rev.* B **75** 140515
[13] Inomata K, Yamamoto T, Billangeon P M, Nakamura Y and Tsai J S 2012 *Phys. Rev.* B **86** 140508
[14] Manucharyan V E, Masluk N A, Kamal A, Koch J, Glazman L I and Devoret M H 2012 *Phys. Rev.* B **85** 024521
[15] Zhu G, Ferguson D G, Manucharyan V E and Koch J 2013 *Phys. Rev.* B **87** 024510
[16] Barends R *et al* 2011 *Appl. Phys. Lett.* **99** 113507
[17] Inomata K, Watanabe M, Yamamoto T, Nakamura Y and Tsai J S 2014 in preparation

[18] Gao J, Daal M, Vayonakis A, Kumar S, Zmuidzinas J, Sadoulet B, Mazin B A, Day P K and Leduc H G 2008 *Appl. Phys. Lett.* **92** 152505
[19] Houck A A *et al* 2008 *Phys. Rev. Lett.* **101** 080502
[20] Yoshihara F, Harrabi K, Niskanen A O, Nakamura Y and Tsai J S 2006 *Phys. Rev. Lett.* **97** 167001
[21] Wellstood F C, Urbina C and Clarke J 1987 *Appl. Phys. Lett.* **50** 772
[22] Kakuyanagi K, Meno T, Saito S, Nakano H, Semba K, Takayanagi H, Deppe F and Shnirman A 2007 *Phys. Rev. Lett.* **98** 047004
[23] Schuster D I, Wallraff A, Blais A, Frunzio L, Huang R S, Majer J, Girvin S M and Schoelkopf R J 2005 *Phys. Rev. Lett.* **94** 123602
[24] Bertet P, Chiorescu I, Burkard G, Semba K, Harmans C J P M, DiVincenzo D P and Mooij J E 2005 *Phys. Rev. Lett.* **95** 257002
[25] Sears A P, Petrenko A, Catelani G, Sun L, Paik H, Kirchmair G, Frunzio L, Glazman L I, Girvin S M and Schoelkopf R J 2012 *Phys. Rev.* B **86** 180504
[26] Schuster D I *et al* 2007 *Nature* **445** 515
[27] Koshino K, Inomata K, Yamamoto T and Nakamura Y 2013 *Phys. Rev. Lett.* **111** 153601
[28] Robertson T L, Plourde B L T, Reichardt P A, Hime T, Wu C E and Clarke J 2006 *Phys. Rev.* B **73** 174526
[29] Kittel C 2005 *Introduction to Solid State Physics* 8th edn (New York: Wiley) chapter 7
[30] Witschel W 1996 *Eur. J. Phys.* **17** 357